

# Superhydrophobicity With Self-Adaptive Water Pressure Resistance and Adhesion of *Pistia Stratiotes* Leaf

Huijuan Shao, Dehui Wang,\* Jianing Song, Zhenxu Shi, Kun Yin, Yang Shen, Bowen Zhang, Luqing Xu, Junchang Guo, Jinlong Yang, and Xu Deng\*

Superhydrophobic surfaces are promising for optimizing amphibious aircraft by minimizing water drag and adhesion. Achieving this involves ensuring these surfaces can resist high liquid pressure caused by deep water and fluid flow. Maximizing the solid-liquid contact area is a common strategy to improve liquid pressure resistance. However, this approach inevitably increases solid-liquid adhesion, making it challenging to guarantee a trade-off between the two wetting characteristics. Here, it is found that the *Pistia stratiotes* leaf exhibits superhydrophobicity with high water pressure resistance and low adhesion, attributed to its self-adaptive deformable microstructure with unique re-entrant features. Under pressure, these microstructures deform to increase the solid-liquid contact area, thereby enhancing water pressure resistance. The re-entrant features elevate the deformation threshold, enabling higher modulus microstructures to achieve adaptive response. This facilitates the recovery of deformed microstructures, restoring the air layer and maintaining low adhesion. Following these concepts, *Pistia stratiotes* leaf-inspired surfaces are fabricated, achieving an 183% improvement in water impact resistance and an  $\approx 80\%$  reduction in adhesion after overpressure compared to conventional superhydrophobic surfaces. The design principles inspired by *Pistia stratiotes* promise significant advancements in amphibious aircraft and other trans-media vehicles.

## 1. Introduction

Air-water trans-media vehicles designed for both underwater and aerial operations, encounter considerable challenges of water drag and water adhesion.<sup>[1]</sup> For example, the amphibious aircraft is confronted with drag skiing on the water<sup>[2,3]</sup> and strong adhesion taking off from water,<sup>[4,5]</sup> which compromises its maximum

take-off weight. To enhance the take-off efficiency of amphibious aircraft, it is crucial to incorporate design considerations aimed at reducing water drag during skiing and minimizing solid-liquid adhesion to facilitate a smooth departure from the water surface. Superhydrophobic surfaces present a promising solution to these challenges. To achieve superhydrophobicity, the surface typically requires rough structures and low surface energy to support stable liquid suspension, creating a Cassie-Baxter state with low solid-liquid contact.<sup>[6,7]</sup> Consequently, this results in diminished drag and solid-liquid adhesion on the submerged superhydrophobic surface,<sup>[8]</sup> optimizing the aircraft's take-off performance.

However, the superhydrophobic surfaces can encounter difficulties in maintaining their air layer at water depths and fluid flow conditions, only withstanding pressure at a depth of 0.03–2.3 meters underwater.<sup>[9–11]</sup> Beyond this range, the air-liquid interface tends to slip and penetrates the surface structures. Various approaches have been explored to address this challenge, such as designing superhydrophobic surfaces with re-entrant structures to increase

the energy barrier for wetting state transitions, thereby strengthening the pressure-resistance.<sup>[12–17]</sup> However, once the air layer on this superhydrophobic surface slides off, it exhibits no recovery, leading to a permanent Wenzel wetting state. Moreover, using nano-scale structures can exhibit two-order-of-magnitude improvement of critical pressure.<sup>[18]</sup> But for achieving significant drag reduction, a slip length on the order of 100  $\mu\text{m}$  is necessary, far exceeding the capabilities of nano-scale structure.<sup>[8]</sup> Another method is to increase the solid-liquid contact area to enhance the resistance to impregnation pressure,<sup>[9,19]</sup> however, it seriously increases the surface's solid-liquid adhesion. Therefore, balancing high pressure resistance and low solid-liquid adhesion on a superhydrophobic surface presents a formidable challenge, as these characteristics often impose conflicting requirements on surface structures.<sup>[20,21]</sup> It has been reported that on superhydrophobic surfaces, the solid-liquid contact area could be altered by water pressure to enhance pressure resistance. Nevertheless, minor alterations in the solid-liquid contact area yield only modest enhancements in pressure resistance.<sup>[19]</sup> Therefore, how to achieve high water pressure resistance and low solid-liquid adhesion on

H. Shao, D. Wang, J. Song, Z. Shi, K. Yin, Y. Shen, B. Zhang, L. Xu, J. Guo, J. Yang, X. Deng  
Institute of Fundamental and Frontier Sciences  
University of Electronic Science and Technology of China  
Chengdu 611731, P. R. China  
E-mail: wangdehui@uestc.edu.cn; dengxu@uestc.edu.cn

J. Song, X. Deng  
Shenzhen Institute for Advanced Study  
University of Electronic Science and Technology of China  
Shenzhen 518110, P. R. China

The ORCID identification number(s) for the author(s) of this article can be found under <https://doi.org/10.1002/adma.202412702>

DOI: 10.1002/adma.202412702

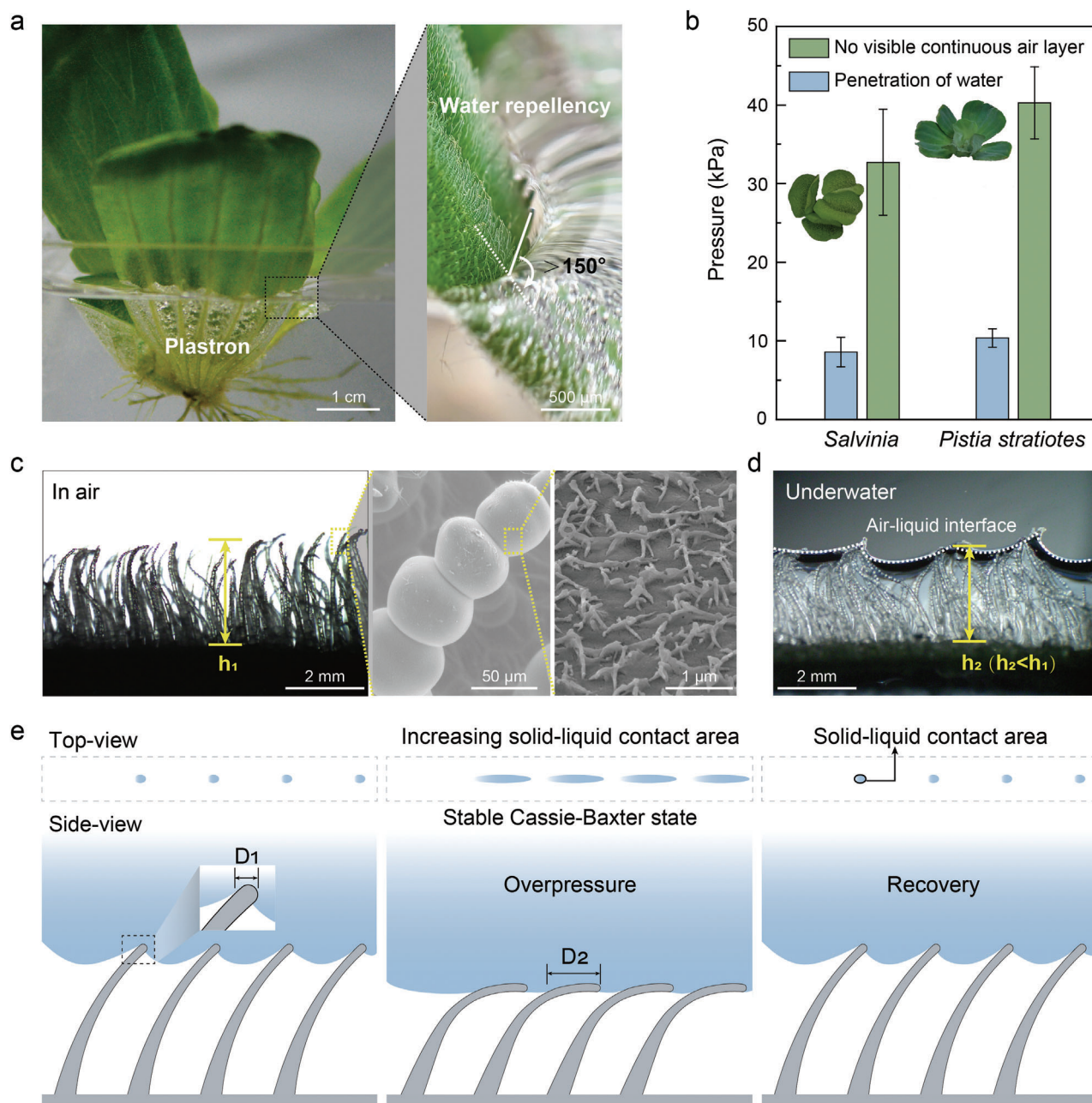


**Figure 1.** The water-repellency of *Pistia stratiotes* leaves surfaces. a) Diagram of *Pistia stratiotes* stably floating on the water with visible plastron, showing excellent water-repellent ability. b) Comparison of air layer retention performance (water-resistance ability) of *Pistia stratiotes* and *Salvinia*. Test process is shown in Figure S1 (Supporting Information). c) Optical photograph and SEM images of the single *Pistia stratiotes* leaf trichomes. The trichomes exhibit re-entrant feature and are covered with nano-particles on the surface. d) Optical photographs demonstrating the self-adaptive deformation phenomenon of *Pistia stratiotes* leaf trichomes. In air, the leaf trichomes of *Pistia stratiotes* are independent of each other. However, the leaf trichomes undergo self-adaptive deformation under water pressure, resulting in the lower height of air layer than that of in air ( $h_2 < h_1$ ). e) Schematic showing self-adaptive pressure stability of *Pistia stratiotes* leaves surfaces. In the side view, the  $D$  (solid-liquid contact) of microstructures obviously increases under overpressure ( $D_1 < D_2$ ).

a superhydrophobic surface is a key challenge in the design of superhydrophobic materials for air-water trans-media applications.

In nature, the aquatic plant *Pistia stratiotes* can float stably on the water, while absorbing enough oxygen, water and sunlight to maintain life, even if there are waves slapping and raindrops hitting.<sup>[22–24]</sup> Under the disturbance of waves and raindrops, the

*Pistia stratiotes* is in a swaying state in the water, while it maintains a stable composite solid-air-liquid interface (Figure 1a). Additionally, when subjected to water impact, the leaves display an excellent water pressure resistance (Video S1, Supporting Information), enduring hydrostatic water pressure up to 40 kPa, higher than that of *Salvinia* (Figure 1b). We found that as

water pressure increasing, the microstructure deforms, increasing the solid-liquid contact area, enhancing the water pressure resistance. As pressure lowering, the deformation of microstructure recovers, reducing the contact area and exhibiting low solid-liquid adhesion. Moreover, we reveal that the re-entrant feature enhances the critical pressure of bioinspired microstructures, which plays a key role in ensuring the deformation of the microstructure. We engineered superhydrophobic surface following the *Pistia stratiotes* wetting mechanism, and this biomimetic surface is capable of dynamically modulating its pressure stability and solid-liquid adhesion, possessing excellent water pressure resistance and water repellency performances. Such advancements are anticipated to significantly enhance the applicability of superhydrophobic surfaces, particularly in the development of air-water trans-media vehicles.

## 2. Self-Adaptive Mechanism: The Collaboration Between the Re-Entrant Features and Deformation

The *Pistia stratiotes* leaf surface has a micro-scale hairy structure with re-entrant feature, which is characterized by nanostructures on their surfaces, as shown in the microscope images (Figure 1c). It provides the necessary rough structures for superhydrophobicity. Further observation, we found that when the hair-like microstructures of leaves are subjected to water pressure, they undergo adaptive deformation (Figure 1d) and maintain a stable air layer. We speculate that the bending deformation of the microstructures notably enhance the contact area as pressure increasing, thereby maintaining their Cassie-Baxter state. Figure 1e illustrates the process of microstructure deformation recovery, specifically the change in contact area. This mechanism also facilitates the restoration of the air layer to its original height following a reduction in water pressure by the deformation recovery, meanwhile maintaining low solid-liquid contact area.

To investigate the mechanism of the self-adaptive pressure resistance and adhesion on *Pistia stratiotes* leaf, we designed hair-like microstructures to mimic the deformation behavior of the leaf structure. Obviously, the bending deformation driving force of the microstructure comes from the pressure exerted on its top (Figure 2a). We define the pressure required to deform the structure as  $P_{def}$ . Based on material modulus and theoretical critical pressure (Figure 2b, Method S1, Supporting Information), COMSOL is employed to model and adjust the micro-structural parameters. This ensures that bending deformation and recovery similar to the microstructures of *Pistia stratiotes* leaf occur under the critical pressure ( $P_{max}$ ). This pressure represents the maximum limit that the Cassie-Baxter wetting state can maintain. The self-adaptive deformation mechanism functions optimally ensue, only if deformation occurs before any slippage at the air-liquid interface, that is  $P_{def} < P_{max}$ . If the  $P_{def}$  exceeds the  $P_{max}$ , deformation cannot occur. In scenarios where the  $P_{max}$  is insufficient, resulting in premature slippage at the air-liquid interface, the self-adaptive deformation cannot respond. Therefore, when  $P_{def}$  is constant, the larger  $P_{max}$  is more likely to undergo self-adaptive mode. The  $P_{max}$  is affected by the structural re-entrant angle and spacing between microstructures, and enlarging the re-entrant angle and reducing the spacing can augment the  $P_{max}$  (Figure 2c,d, Equations S1, S2, Supporting Information). Therefore, the re-entrant feature of *Pistia stratiotes* leaf

microstructures is to enhance their ability to deform, allowing them to better cooperate with the deformation to resist water pressure.

To prove this mechanism, artificial leaf microstructures were designed and fabricated with various re-entrant angles (Figures S2,S3,S4, Supporting Information) and staggered arrangement with different spacings (Figure 2e; Figure S5, Supporting Information), microstructures fabricated using PDMS or epoxy resin with varying moduli. As illustrated in Figure 2f, testing by home-made water-resistance equipment<sup>[25]</sup> (Figure S6, Supporting Information), PDMS elastomer microstructures with re-entrant features exhibit microstructures more readily deform, maintaining a stable air layer. The PDMS microstructures without re-entrant features are impaled by water and transfer from Cassie to Wenzel state. This indicates the re-entrant features of microstructures can facilitate the deformation, maintaining a stable wetting state. Moreover, the larger re-entrant angle and greater top radii further contribute to an enhanced resistance against water pressure (Figure S7, Supporting Information). On the other hand, according to the formula in  $\delta = P \frac{64L^3}{3\pi E(2R)^4}$  (Figure 2a, Equations S3, S4, Supporting Information),<sup>[26,27]</sup> microstructures with a higher  $E$  value result in smaller displacement distances, and vice versa, also evidenced in Figures S8, S9; Method S2 (Supporting Information). Therefore, to have a deeper comprehension of the variables influencing the bending deformation, we fabricated PDMS microstructures with different cross-linker mass ratios (different Young's modulus). As described by the equation the  $P_{max} = 2\pi R\gamma \sin(\theta + \alpha - \pi)/D^2(1-f)$  (Equation S2, Supporting Information).<sup>[28]</sup> When the solid-liquid contact area fraction ( $f$ ) decreases, the  $P_{max}$  drops, making the air-liquid interface prone to slipping, impaling the interface, and inhibiting the deformation of microstructures. To ensure that the microstructure can deform to increase the solid-liquid contact area fraction when subjected to pressures higher than the  $P_{max}$ , the modulus  $E$  of microstructures can also be reduced, or the space  $D$  can be reduced, as shown in Figure 2g. Especially, incorporating the re-entrant features enables higher modulus microstructures to achieve adaptive deformation (Figure 2g). Additionally, a higher modulus indicating better elasticity (Figure S10, Supporting Information) aids in the recovery of deformation in the PDMS microstructures. However, a lower modulus hinders the recovery (Figure S11, Supporting Information), after pressure relieving, it is difficult for the microstructure to return to its original position, which is not conducive to the restoration of the air layer (Figure 2h). Obviously, for indeformable resin microstructure (Control), the height of air layer noticeably declines due to the escape of air, with no recovery, as shown in Figure 2h and Video S2 (Supporting Information), although there is no significant difference in static hydrophobicity among them (Figure S12, Supporting Information). Besides, the recyclability of the microstructures has been confirmed, and the experimental results indicate that after 10 cycles, the self-adaptive deformation-recovery performance of microstructures shows no significant decline (Figure S13, Supporting Information). Overall, the re-entrant feature aids in increasing the  $P_{max}$ , facilitating the deformation of microstructures. Further, the self-adaptive deformation enhances the water pressure resistance of superhydrophobic surfaces, and thereby augments the water pressure resistance.



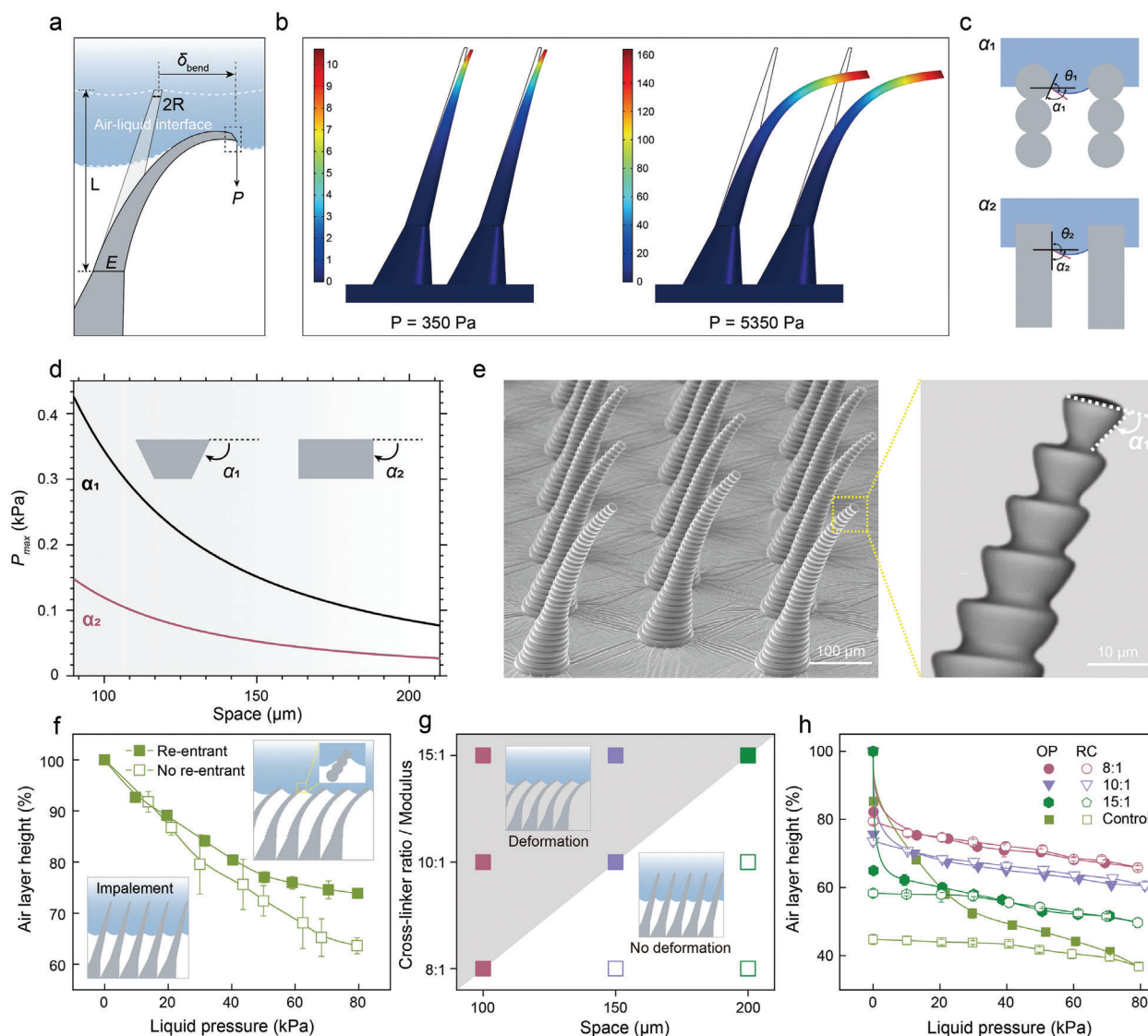


**Figure 2.** The collaboration between the re-entrant features and deformation a) Schematic diagram showing the force analysis of micropillar.  $P$  is the total force experienced by the microstructures. More details are in Supplementary text 2. b) COMSOL simulation showing the deformation of microstructures when subjected to pressure. Deformation is positively correlated with the pressure. c) Diagram showing the equilibrium contact angle ( $\theta$ ) and re-entrant angles ( $\alpha_1$  of  $150^\circ$  and  $\alpha_2$  of  $90^\circ$ ) of two structures. d) Relationship between critical pressure ( $P_{\text{max}}$ ) and space for microstructures with two different re-entrant angles ( $\alpha_1$  and  $\alpha_2$ ). The  $\theta$  is set as  $110^\circ$ . e) The PDMS microstructure surfaces showing multi-re-entrant microstructures with re-entrant angle of  $\alpha_1$ . f) The air layer height (%) of PDMS (cross-linker ratio of 8:1) microstructures surfaces with re-entrant features and PDMS microstructures surfaces without re-entrant features. g) Influence of space and modulus on bending deformation of microstructures. We varied the Young's modulus by adjusting the mass ratio of polydimethylsiloxane (PDMS) pre-polymer to curing agent. The PDMS with mass ratios of 8:1, 10:1, and 15:1 correspond to Young's moduli of 3.78, 3.30, and 1.14 MPa, respectively, more details are provided in Table S1 (Supporting Information). PDMS microstructures with different moduli have different performance of bending deformation. Notably, at a  $100 \mu\text{m}$  spacing, microstructures of all moduli are able to bend successfully; at a  $150 \mu\text{m}$  spacing, only the microstructures with Young's moduli of 10:1 and 15:1 can bend; and at a  $200 \mu\text{m}$  spacing, only the microstructures with 15:1 modulus are bendable. h) Variation of air layer height (%) under overpressure-recovery (OP-RC) conditions. The specific test conditions involved increasing the pressure from 0 to 80 kPa and then decreasing back to 0 kPa. For bioinspired microstructure surfaces, more details are in Video S2 (Supporting Information).

### 3. Self-Adaptive Deformation Contributes to Enhanced Pressure Resistance and Low Adhesion Retention

As shown in Figure 3a, Figure S14 (Supporting Information), with pressure increasing and then relieving, the water is al-

ways suspended at the top of the microstructures, maintaining a Cassie-Baxter state and exhibiting self-adaptive pressure resistance performance. However, for indeformable resin microstructures (Control), bubbles escape, and the air-liquid interface is penetrated by water, resulting in irreversibility of the air layer (Figure 3b). Moreover, by utilizing the optical reflection method,

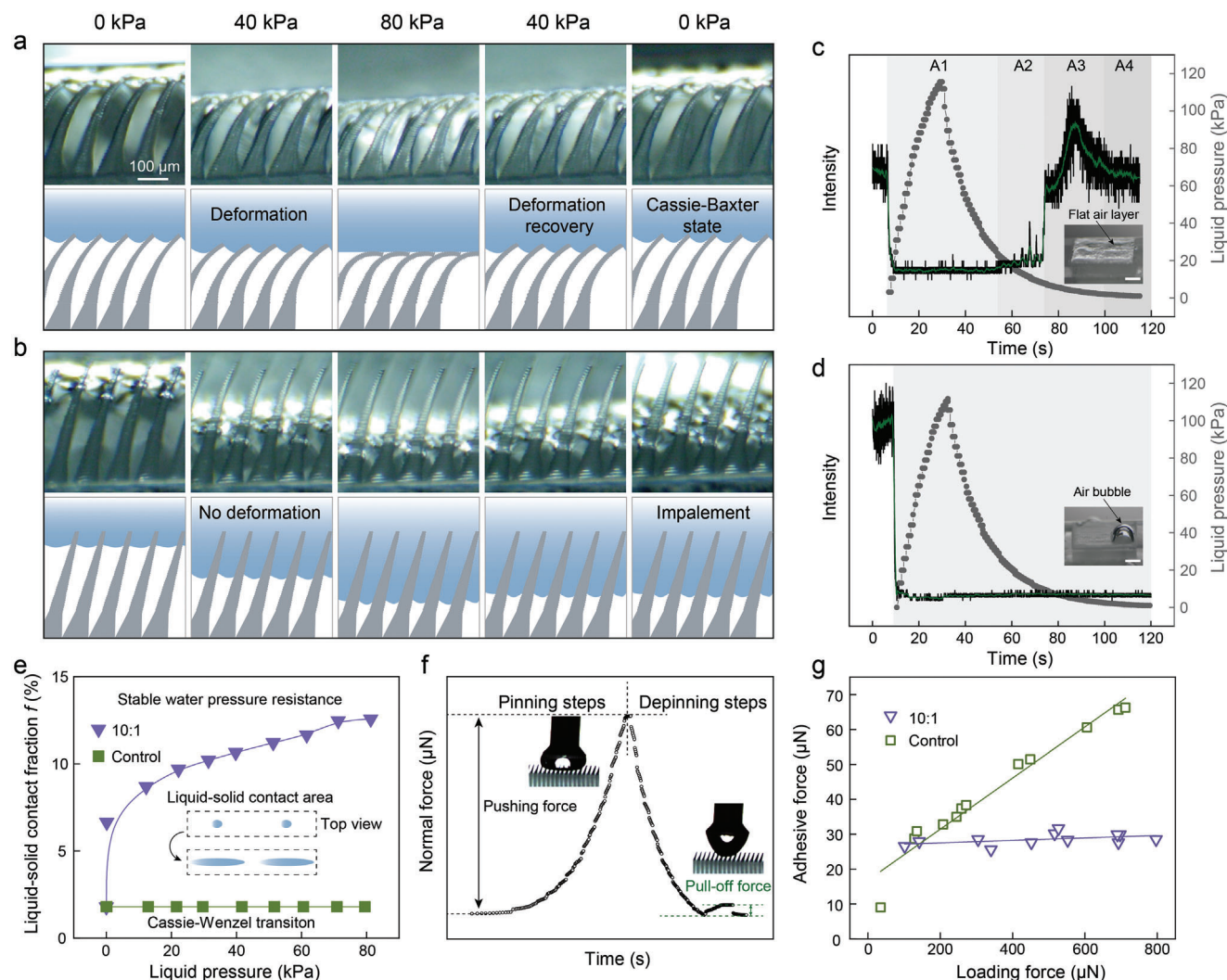


**Figure 3.** *Pistia stratiotes* inspired self-adaptive pressure resistance and adhesion. a) Side-view optical photography and schematic diagram of PDMS microstructures surfaces with cross-linker ratio of 10:1 under OP-RC conditions. b) Side-view optical photography and schematic diagram of indeformable resin microstructures under OP-RC conditions. c) The air layer recovery performance of PDMS microstructures surfaces with cross-linker ratio of 10:1 detected by the reflected light intensity. The first stage (A1) is the disappearance of the air layer as pressure increases, the second stage (A2) is the gradual recovery of the air layer height, the third stage (A3) involves disturbances in the air layer caused by the recovery of micropillars' bending deformation, and the fourth stage (A4) is the recovery of the air layer to its initial condition. Scale bar: 2 mm. d) Changes in optical intensity of indeformable resin microstructures surfaces (Control) with water pressure, demonstrating the irreversibility of air layer. Scale bar: 2 mm. e) The liquid-solid contact area fraction changes with increasing the liquid pressure. Inserted diagram shows the deformation of microstructures and the change of solid-liquid contact line. f) Schematic of dynamic adhesive force measurement of superhydrophobic surface. g) Adhesive force-loading force curve of PDMS microstructures surfaces with cross-linker ratio of 10:1 and indeformable resin microstructures (Control).

it can explicitly showcase the capability to restore the air layer on superhydrophobic surfaces (more details are in Figure S15, Equation S5, Supporting Information). As the pressure increases, the optical intensity of PDMS elastomer microstructures diminishes and eventually returns to their initial level, demonstrating the stability of air-liquid interface and recoverability of air layer height (Figure 3c). For comparison, the optical intensity of indeformable resin microstructures merely exhibits a decreasing trend with on recovery (Figure 3d), and their air layer also diminishes more rapidly compared to that of PDMS microstructure (Figure S16, Supporting Information), due to their inability to deform. Actually, all the differences are attributed to the

changes in contact area, which affects the ability to resist liquid infiltration of surfaces. To assess the evolution of the solid-liquid contact area fraction ( $f$ ) of surfaces under increasing hydrostatic pressure, we conducted an analysis based on the height of air layer and micropillars' dimensions (Method S3, Supporting Information). As depicted in Figure 3e, Figure S17 (Supporting Information), the contact area fraction of the PDMS microstructure surfaces with cross-linker ratio of 10:1 is 6 times larger than that of indeformable resin microstructures under 80 kPa. Meanwhile, it expands with rising hydrostatic pressure, thereby increasing the water pressure resistance of superhydrophobic surfaces.

Unlike traditional superhydrophobic surfaces which cannot balance both pressure stability and low solid-liquid adhesion,<sup>[29,30]</sup> the *Pistia stratiotes* inspired microstructure surfaces can retain relatively low adhesion after water pressure relieving. We utilized a high-precision balance to study the variations in dynamic adhesive force. The testing process for dynamic adhesive force mainly consists of two stages. The first stage is the droplet movement stage, where the droplet continues to move downward after initially contacting the surface. The second stage is the droplet detaching from the surface stage, during which the microstructure of the surface induces a pinning effect on the droplet, thereby generating an adhesive force, as seen in Figure 3f. By adjusting the displacement of droplets, we can alter the pressure exerted on the surface to examine adhesive force behavior under diverse pressure conditions. As the pressure applied to the superhydrophobic surfaces increases, the adhesive force of the PDMS microstructure surfaces with cross-linker ratio of 10:1 remain relatively constant, whereas the adhesive force of the indeformable resin microstructures (Control) demonstrates a linear increase, surpassing that of the PDMS microstructure (Figure 3g; Figure S18, Supporting Information). According to  $F \sim 2\pi r \gamma \cos^2 \frac{\theta}{2} l/d$  (Equations S6, S7, Supporting Information),<sup>[31,32]</sup> we conclude this divergence can be attributed to the behavior of microstructures under pressure. Specifically, for PDMS microstructure, the contact area of microstructures changes dynamically with pressure and remains in a Cassie-Baxter wetting state, and the contact line returns to its initial state when the droplet is removed from the surface, hence adhesive forces were always low. Conversely, the indeformable resin microstructures experienced droplet penetration, transitioning to a Wenzel state, which enlarged the contact line,<sup>[31,32]</sup> thus necessitating higher adhesive forces for droplet extraction.

#### 4. Performance of the *Pistia Stratiotes* Inspired Superhydrophobic Surfaces

To verify the water pressure-resistance for potential applications, we further developed a *Pistia stratiotes* inspired self-adaptive superhydrophobic surfaces with re-entrant feature coated with nano particles (Figure S19, Supporting Information). The surfaces exhibit droplet-repellent properties, including water contact angle of 156° and rolling angle of 4° (Table S2, Supporting Information), as well as effective droplet rebound performance (Figure S20, Method S4, Supporting Information). The hydrostatic water pressure resistance assessments show that the maximum pressure resistance of self-adaptive superhydrophobic surfaces reaches ≈91 kPa, which is equivalent to being 9 meters deep underwater, significantly higher than that of indeformable superhydrophobic surfaces, demonstrating its superior hydrostatic pressure resistance performance (Figure 4a; Figure S21, Supporting Information). Moreover, superhydrophobic materials always need to face the impact of dynamic water pressure on their application underwater,<sup>[33,34]</sup> for instance, the water impact on the amphibious aircraft occurs both when it accelerates to take off and lands on water.<sup>[3]</sup> Therefore, we assessed the resistance of self-adaptive superhydrophobic surfaces in fluid systems by applying nitrogen gas at different pressures to drive the water flow across the surface, and the integrity of the air layer monitored

indicates that with increasing gas pressure (Figure S22, Supporting Information), the optical intensity of self-adaptive superhydrophobic surfaces would suddenly decrease and then recover, implying that the air layer can rapidly restore after the impact of water flow (Figure 4b). Higher gas pressures, which indicate higher flow rates or water pressure, demonstrate the surface's strong ability to maintain its superhydrophobic state.<sup>[33,35]</sup> The self-adaptive superhydrophobic surfaces could withstand water flow impact up to 0.34 MPa of gas pressure, ≈183% higher than that of the indeformable superhydrophobic surfaces (0.12 MPa) which are unable to deform (Figure 4b). These results are also supported by confocal microscopy (Method S3, Supporting Information), as shown in Figure 4c, after being subjected to water impacting with 0.32 MPa gas pressure, the self-adaptive superhydrophobic surfaces still maintain a stable air layer (yellow part). In contrast, the air layer of indeformable superhydrophobic surfaces nearly disappears at 0.12 MPa gas pressure, indicating that the air layer is swept away by the water. Further, to accurately simulate the conditions experienced by an air-water trans-media vehicle, first, the samples undergo underwater overpressure to imitate the water pressure encountered during skiing. Subsequently, we pull the samples from the water to simulate the take-off from water (Figure S23, Supporting Information). After overpressure, as displayed in Figure 4d, the adhesive force of self-adaptive superhydrophobic surface is ≈80% lower than indeformable superhydrophobic surface, as illustrated in Figure 4e, and Method S5 (Supporting Information). Physical photographs show that self-adaptive superhydrophobic surface displays no water adhesion. In contrast, indeformable superhydrophobic surface which achieves solid-liquid separation from the water surface, presents a noticeable water film and water drag (Figure 4f).

#### 5. Conclusion

We present that the aquatic plant *Pistia stratiotes* exhibits self-adaptive water pressure resistance and low solid-liquid adhesion. This is achieved by altering the solid-liquid contact area through deformation and recovery of its microstructures with re-entrant features. Only the microstructures deform prior to the sliding of the air-liquid interface, transitioning into a self-adaptive response for water pressure resistance. The re-entrant feature enhances the deformation threshold which promotes microstructures' deformation and allows for the use of higher modulus microstructures, resulting in the recovery of the air layer. Meanwhile, the deformation recovery of microstructures leads to the recovery of solid-liquid contact area, maintaining low solid-liquid adhesion. Following these concepts, we fabricate *Pistia stratiotes* leaf-inspired surfaces, which are capable of balancing high pressure resistance and low solid-liquid adhesion. Such advancements are anticipated to significantly enhance the applicability of superhydrophobic surfaces, particularly in the development of air-water trans-media vehicles, such as amphibious aircraft.

#### 6. Experimental Section

**Materials:** *Pistia stratiotes* was purchased from Fujian province, China, and farmed in laboratory at constant temperature. *Pistia stratiotes* leaves used in experiments were collected from fresh plant.



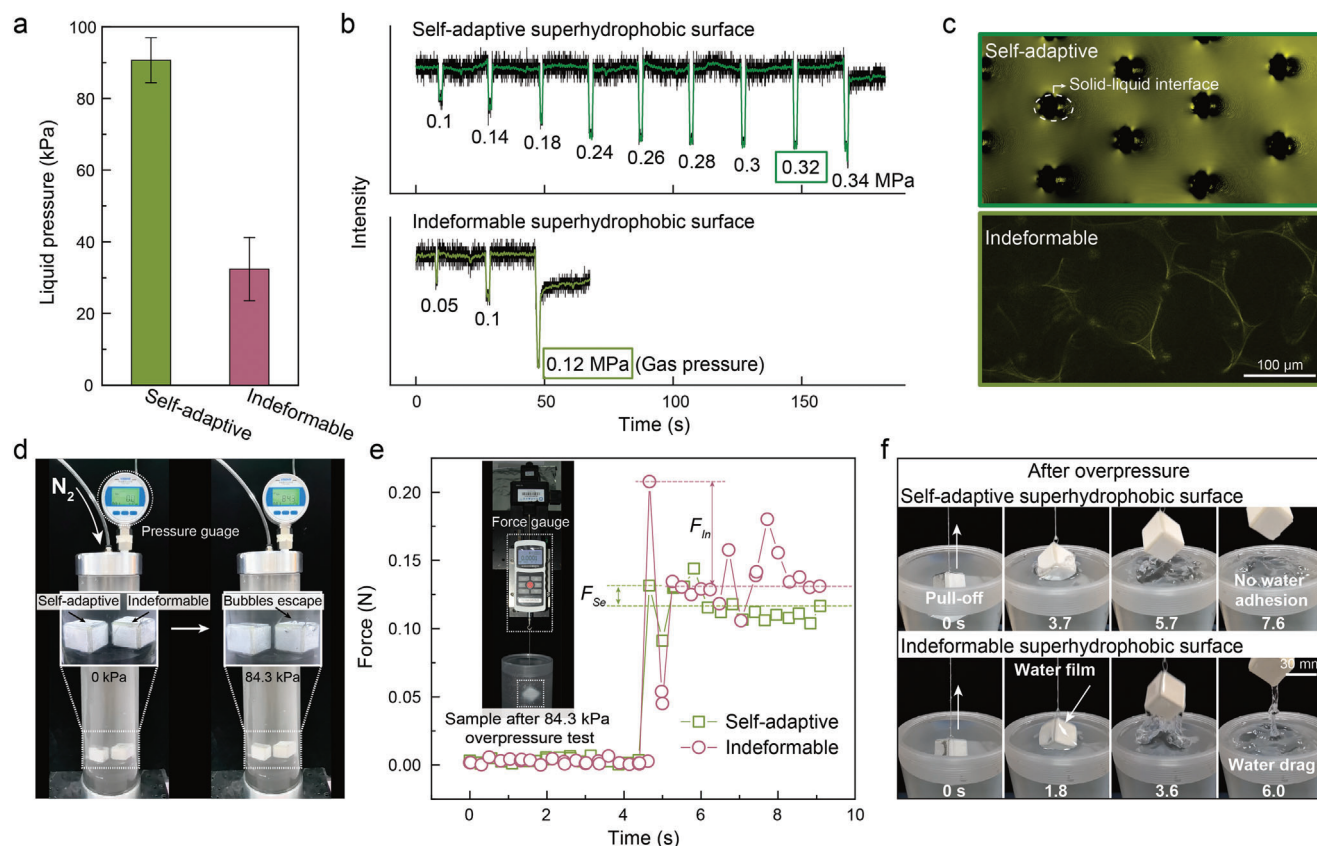


**Figure 4.** Application of *Pistia stratiotes* inspired self-adaptive superhydrophobic surfaces. a) Comparison of hydrostatic water pressure resistance of *Pistia stratiotes* inspired self-adaptive superhydrophobic surface and indeformable superhydrophobic surface. We define the maximum hydrostatic pressure as the threshold that the surface displays no visible silvery air layer. b) The water pressure resistance of self-adaptive superhydrophobic surface and indeformable superhydrophobic surface with gas pressure increasing. c) The confocal microscopy images of self-adaptive superhydrophobic surface and indeformable superhydrophobic surface after water impacting at 0.32 and 0.12 MPa gas pressure, respectively. The solid-liquid interface is the black part, and the yellow part is the air-liquid interface. d) The overpressure test process of self-adaptive superhydrophobic surface and indeformable superhydrophobic surface. After 84.3 kPa water pressure, bubbles are observed escaping from the indeformable superhydrophobic surface. e) The adhesive forces curve of the self-adaptive superhydrophobic surface and indeformable superhydrophobic surface, simulating the take-off process of an amphibious aircraft after 84.3 kPa overpressure. The water adhesion forces of the self-adaptive superhydrophobic surface and the indeformable superhydrophobic surface are denoted as  $F_{Se}$  and  $F_{In}$ , respectively. More details are in Video S3, Method S5 (Supporting Information). f) The photographs show the self-adaptive superhydrophobic surface and indeformable superhydrophobic surface detaching from water surface after being subjected to 84.3 kPa water pressure.

**Fabrication of Leaf Microstructure Surfaces:** Samples templates were fabricated by projection micro stereolithography 3D printing technique (BMF PRECISION TECH, nanoArch S140). The printing material is the photosensitive resin cured at 405 nm. Polydimethylsiloxane (PDMS) precursor (Sylgard 184A) and curing agent (Sylgard 184B) were purchased from Dow Corning Corporation, U. S. A. The precursor and curing agent were set at a mass ratio of 15:1. The above-mentioned mixed PDMS solutions were poured on the template and degassed in a vacuum oven for 20 min, and then was cured at 60 °C for 4 h. Next, the cured PDMS negative template was peeled from the positive template. The negative template was performed fluorination to form an anti-sticker layer. Finally, a second positive replication was fabricated on the treated negative replicas following the same method as above with PDMS precursor and curing agent of 8:1, 10:1 and 15:1. To fabricate indeformable micropillar surfaces, epoxy resin (Lishibang) with precursor and curing agent of 3:1 was used. For practical application of the leaf microstructure surfaces, all the surfaces were coated with nanoparticles with commercial Glaco.

**Characterization of PDMS Samples:** The Young's modulus and Poisson's ratio of PDMS were measured following ASTM D412 using a universal material testing machine (Instron, model 5943, USA). The feed rate is

5 mm min<sup>-1</sup>. The sample length is 115 mm, the width is 6 mm, and the thickness is 3 mm. The Poisson's ratio value is the radial strain  $\epsilon_R$  to the longitudinal strain  $\epsilon_L$ .

**Rheology Measurement of PDMS Samples:** The viscoelastic properties of PDMS materials were measured using the DMA tester (Q850 DMA, TA Instruments) in the compression mode at 0.1–100 Hz. The test chamber's temperature was set at 25 °C. The test specimens were prepared with a Teflon mold with 1.5 cm diameter and 0.5 cm depth. PDMS solutions with precursor-curing agents of 8:1, 10:1 and 15:1 were filled the mold following degassing in a vacuum oven and cured at 80 °C for 4 h.

**Characterization of the Leaf Microstructure Surfaces:** The water contact angle and roll-off angle were measured with a contact angle measuring instrument (OCA 50 AF, Dataphysics, Germany). The static contact angle was measured by dispensing a sessile drop of 5  $\mu$ L with a pipette on the test samples and calculated by software. The roll-off angles were tested by dispensing 10  $\mu$ L onto the test surface. The tilting rate was set at a speed of 5° per second until the droplet rolled off the surface. The roll-off angles were recorded by goniometer. All the data were duplicated three times.

**Morphologies Measurement of Samples:** The surface morphologies of samples were characterized using a scanning electron microscope

(Quattro S, Thermo Fisher, USA) operating at 10 kV. All the test samples were sprayed with gold (Magnetron Ion Sputter Metal Coating Device, MSP-2S, Japan) for 3 min before the test.

**Test of Air Layer Retention and Restoration under Overpressure-Recovery Conditions:** A homemade device consists of two thick pieces of transparent glass with a plug and pressure gauge. The samples were pressurized by injecting nitrogen into the device. High-speed camera (FASTCAM NOVAs16, Photron, Japan) was used to record the air layer height of samples under overpressure-recovery conditions. The lens of the high-speed camera was perpendicular to the cross-section of the test samples. The water pressure was recorded by a pressure online monitoring software. The ratio of the height of the air layer under overpressure to the physical height of the micropillar was defined as the air layer percentage, which was written as the air layer height in this study.

**Dynamic Adhesion Force Measurement:** The dynamic adhesion of the sample was measured using a highly sensitive electric Y-axis mobility control platform (42M-1.8D, Zolix, China) and 1/10 000 electronic balance (ME55/02, METTLER TOLEDO, Switzerland). A droplet with a volume of 2  $\mu\text{L}$  was suspended on a microcolumn with a diameter of 1.5 mm. The microcolumn was moved slowly until the droplet touched the sample surface. To apply different forces to the sample surface, we controlled the distance of the droplet pressing. The movement speed of the droplet was set 0.1 mm  $\text{s}^{-1}$ . During the process of droplet pressing down on the surface, the pressure on the sample surface gradually increased. Then the droplet was withdrawn from the surface at the same speed. At this time, the force exerted by the surface on the droplet was the adhesion force, and this value recorded by the balance was negative.

**Reflection Measurement of the Air Layer on Samples Surfaces Underwater:** The test sample was placed in a sealed pressurized chamber or a pipe designed for high-speed water impact. The length, width and height of the chamber are 3 cm, 8 and 3 mm. The tube connecting the chamber was 4 mm in diameter and 1 mm in wall thickness. A 532 nm laser beam was used to illuminate the sample surface (the surface air layer), and the beam was reflected by the air layer of the sample surface. The light intensity was detected by the photosensor with suitable angle to collect sufficient light intensity. Finally, the light intensity detected by photosensor was converted into voltage and displayed on the oscilloscope (RTE 1022, Rohde & Schwarz, America). When the laser was not applied, the voltage was set as the baseline. Once the photosensor detects laser irradiation, the voltage starts to either increase or decrease in response to the changes in the height of the air layer, with the voltage resulting value being positive. In this study, the optical reflection method to assess the recovery of the air layer on surfaces was primarily used. Therefore, instead of comparing specific values, it mainly focused on the overall trend of the final voltage intensity. More details were in Text S4 (Supporting Information).

## Supporting Information

Supporting Information is available from the Wiley Online Library or from the author.

## Acknowledgements

The authors acknowledge funding support by the National Natural Science Foundation of China (52103136, 22275028, U22A20153, 22325201), the Shenzhen Science and Technology Program (JCYJ20210324142210027), the Sichuan Science and Technology Program (2023)DRC0082).

## Conflict of Interest

The authors declare no conflict of interest.

## Data Availability Statement

The data that support the findings of this study are available from the corresponding author upon reasonable request.

## Keywords

*Pistia stratiotes*, pressure resistance, self-adaptive, solid-liquid adhesion, superhydrophobic surfaces

Received: August 26, 2024

Revised: October 25, 2024

Published online:

- [1] L. Qiu, W. Song, *J. Aircraft* **2013**, *50*, 1369.
- [2] X. Duan, W. Sun, C. Chen, M. Wei, Y. Yang, *Aerosp. Sci. Technol.* **2019**, *84*, 980.
- [3] H. Zhou, K. Hu, L. Mao, M. Sun, J. Cao, *Ocean Eng.* **2023**, *272*, 113848.
- [4] Y. Lu, S. Deng, Y. Chen, T. Xiao, J. Chen, F. Liu, S. Song, B. Wu, *J. Aircraft* **2024**, *61*, <https://doi.org/10.2514/1.C037660>.
- [5] H. Sun, A. Ju, W. Chang, J. Liu, J. Liu, H. Sun, *J. Marine Sci. Engineer.* **2024**, *12*, 585.
- [6] M. Liu, Y. Zheng, J. Zhai, L. Jiang, *Acc. Chem. Res.* **2010**, *43*, 368.
- [7] Y. Lu, S. Sathasivam, J. Song, C. R. Crick, C. J. Carmalt, I. P. Parkin, *Science* **2015**, *347*, 1132.
- [8] C. Lee, C.-H. Choi, C.-J. Kim, *Experiments in Fluids* **2016**, *57*, 176.
- [9] Q. S. Zheng, Z. H. Zhao, *Langmuir* **2005**, *21*, 12207.
- [10] B. Emami, T. M. Bucher, H. V. Tafreshi, D. Pestov, M. Gad-el-Hak, G. C. Tepper, *Colloids Surf., A* **2011**, *385*, 95.
- [11] W. Choi, M. Kang, J. Y. Park, H. E. Jeong, S. J. Lee, *Phys. Fluids* **2021**, *33*, 022001.
- [12] Z. Dong, P. A. Levkin, *Adv. Funct. Mater.* **2023**, *33*, 2213916.
- [13] G. T. Yun, W. B. Jung, M. S. Oh, G. M. Jang, J. Beak, N. I. KIM, S. G. Im, H. T. Jung, *Sci. Adv.* **2018**, *4*, eaat4978.
- [14] P. Sun, Y. Jin, Y. Yin, C. Wu, C. Song, Y. Feng, P. Zhou, X. Qin, Y. Niu, Q. Liu, J. Zhang, Z. Wang, X. Hao, *Small Methods* **2023**, *8*, 2201602.
- [15] J. Li, X. Han, W. Li, L. Yang, X. Li, L. Wang, *Prog. Mater. Sci.* **2023**, *133*, 101064.
- [16] J. Sun, P. Zhu, X. Yan, C. Zhang, Y. Jin, X. Chen, Z. Wang, *Appl. Phys. Rev.* **2021**, *8*, 031403.
- [17] X. Liu, H. Gu, M. Wang, X. Du, B. Gao, A. Elbaz, L. Sun, J. Liao, P. Xiao, Z. Gu, *Adv. Mater.* **2018**, *30*, 1800103.
- [18] B. Liu, F. F. Lange, *J. Colloid Interface Sci.* **2006**, *298*, 899.
- [19] Y. Tan, J. Yang, Y. Li, X. Li, Q. Wu, Y. Fan, F. Yu, J. Cui, L. Chen, D. Wang, X. Deng, *Adv. Mater.* **2022**, *34*, 2202167.
- [20] A. Tuteja, W. Choi, M. Ma, J. M. Mabry, S. A. mAZZELLA, G. C. Rutledge, G. H. McKinley, R. E. Cohen, *Science* **2007**, *318*, 1618.
- [21] C. J. Kim, T. Liu, *Science* **2014**, *346*, 1102.
- [22] Y. Ma, F. Zhao, L. Wang, Y. Ding, H. Zhao, H. Wang, J. Liu, *RSC Adv.* **2021**, *11*, 18783.
- [23] Y. Yang, H. Bai, M. Li, Z. Li, X. Wang, P. Wang, M. Cao, *Mater. Horiz.* **2022**, *9*, 1888.
- [24] F. Vullers, G. Gomard, J. B. Preinfalk, E. Klampaftis, M. Worgull, B. Richards, H. Holscher, M. N. Kavalenka, *Small* **2016**, *12*, 6144.
- [25] Y. Zhang, Y. Hu, B. Xu, J. Fan, S. Zhu, Y. Song, Z. Cui, H. Wu, Y. Yang, W. Zhu, F. Wang, J. Li, D. Wu, J. Chu, L. Jiang, *ACS Nano* **2022**, *16*, 2730.
- [26] I. Schoen, W. Hu, E. Klotzsch, V. Vogel, *Nano Lett.* **2010**, *10*, 1823.
- [27] Y. Jiang, Z. Xu, B. Li, J. Li, D. Guan, *Langmuir* **2023**, *39*, 15401.
- [28] A. Tuteja, W. Choi, J. M. Mabry, G. H. McKinley, R. E. Cohen, *Proc. Natl. Acad. Sci. USA* **2008**, *105*, 18200.
- [29] P. Papadopoulos, L. Mammen, X. Deng, D. Vollmer, H. J. Butt, *Proc. Natl. Acad. Sci. USA* **2013**, *110*, 3254.
- [30] Y. Lai, X. Gao, H. Zhuang, J. Huang, C. Lin, L. Jiang, *Adv. Mater.* **2009**, *21*, 3799.



- [31] J. Yang, D. Wang, H. Liu, L. Li, L. Chen, H. R. Jiang, X. Deng, *Lab Chip* **2019**, *19*, 1296.
- [32] M. Ye, X. Deng, J. Ally, P. Papadopoulos, F. Schellenberger, D. Vollmer, M. Kappl, H. J. Butt, *Phys. Rev. Lett.* **2014**, *112*, 016101.
- [33] Y. Xiang, Y. Xue, P. Lv, D. Li, H. Duan, *Soft Matter* **2016**, *12*, 4241.
- [34] X. Li, J. Yang, K. Lv, P. Papadopoulos, J. Sun, D. Wang, Y. Zhao, L. Chen, D. Wang, Z. Wang, X. Deng, *Natl. Sci. Rev.* **2021**, *8*, nwaa153.
- [35] W. Cho, S. Heo, S. J. Lee, *Phys. Fluids* **2022**, *34*, 122115.